Atomic structure and stability of magnetite $Fe_3O_4(001)$: an x-ray view

Björn Arndt[a,b], Roland Bliem[c], Oscar Gamba[c], Jessi E. S. van der Hoeven[d], Heshmat Noei[a], Ulrike Diebold[c], Gareth S. Parkinson[c], Andreas Stierle[a,b,*]

[a] *Deutsches Elektronen-Synchrotron (Desy), Notkestraße 85, D-22607 Hamburg*
[b] *University of Hamburg, D-20355 Hamburg*
[c] *Institute of Applied Physics, Wiedner Hauptstrasse 8-10, Vienna University of Technology, 1040 Vienna, Austria*
[d] *Debye Institute for Nanomaterials, Utrecht University, 3508 TA Utrecht, The Netherlands*

Abstract

The structure of the $Fe_3O_4(001)$ surface was studied using surface x-ray diffraction in both ultra-high vacuum, and higher-pressure environments relevant to water-gas shift catalysis. The experimental x-ray structure factors from the $\sqrt{2}$x$\sqrt{2}$R45° reconstructed surface are found to be in excellent agreement with the recently proposed subsurface cation vacancy (SCV) model for this surface (Science 346 (2014), 1215). Further refinement of the structure results in small displacements of the iron atoms in the first three double layers compared to structural parameters deduced from LEED I-V experiments and DFT calculations. An alternative, previously proposed structure, based on a distorted bulk truncation (DBT), is conclusively ruled out. The lifting of the $\sqrt{2} \times \sqrt{2}$R45° reconstruction upon exposure to water vapor in the mbar pressure regime was studied at different temperatures under flow conditions, and a roughening of the surface was observed. Addition of CO flow did not further change the roughness perpendicular to the surface but decreased the lateral correlations.

1. Introduction

Magnetite is an interesting material due to its surface reactivity, as well as its exceptional electronic and magnetic properties. It is involved in the catalysis of the water-gas shift reaction [1], in Fischer-Tropsch synthesis [2], and it also raised some interest due to its possible application for groundwater remediation [3] and in spintronic devices [4]. Since these applications depend on the surface structure of the material, a correct description is fundamental for a deeper understanding of the processes involved. Magnetite crystallizes in the inverse spinel structure, which can be described as a distorted oxygen fcc lattice with iron ions filling one eighth of the octahedral and one sixteenth of the tetrahedral positions [5]. The tetrahedrally coordinated iron ions (Fe_{tet}) are formally in a Fe^{3+} charge state, and the octahedral sites (Fe_{oct}) are equally filled by Fe^{2+} and Fe^{3+}. Under ultrahigh vacuum (UHV) conditions, the clean (001) surface of magnetite exhibits a $\sqrt{2} \times \sqrt{2}$R45° reconstruction [6–10]. As a result of a combined study by density functional theory (DFT), low energy electron diffraction (LEED) current - voltage (I-V) measurements and surface x-ray diffraction (SXRD), it was proposed that the surface is bulk truncated at the B layer (a plane containing both Fe_{oct} and O atoms, see Fig. 1a). In this distorted bulk truncation (DBT) model, a Jahn-Teller distortion of the octahedrally coordinated iron ions in the surface leads to a wave-like displacement of the surface oxygen-iron rows [11, 12], in qualitative agreement with contrast observed in STM images. LEED I-V and SXRD experiments were concluded to confirm the structure. Recently however, a new model was

*Corresponding author.
Email address: andreas.stierle@desy.de (Andreas Stierle)

proposed [13] based on an ordered array of Fe_{oct} subsurface cation vacancies and Fe_{tet} surface interstitials (SCV model). The Pendry r-factor achieved in LEED I-V data analysis was significantly improved (0.125) over the DBT model (0.34), and DFT+U calculations suggest the SCV model is thermodynamically more stable than the DBT model [13].

Here we present an extended SXRD dataset from the $\sqrt{2} \times \sqrt{2}$R45° surface in comparison to a previous SXRD study [11]. Structure factors extracted from the data were used to compare and refine the different models. Ultimately, our results confirm the recently proposed SCV model of the reconstructed surface.

In addition to the clean surface, the evolution of the surface structure in a water vapor rich environment is important because magnetite is used as a catalyst for the water-gas shift reaction [1]. Water adsorption on magnetite (001) has been studied previously at varying pressure ranges by STM [14], LEED I-V [15], XPS [16, 17], and using DFT+U calculations [15, 17, 18]. Interestingly, exposure to 10^{-6} mbar water vapor at 273 K was reported to lift the $\sqrt{2} \times \sqrt{2}$R45° reconstruction, and a mixed-mode adsorption containing both dissociated and intact water molecules was proposed on the basis of LEED I-V and DFT+U calculations.

In this study, we apply surface x-ray diffraction (SXRD) to investigate changes that occur at the (001) surface of magnetite at near atmosphere pressures and temperatures. We followed the lifting of the surface reconstruction in water vapor and show that the exposure to water vapor at 520 K is concomitant with a roughening of the surface. Heating under a combined CO and water vapor flow at higher temperature leads to a decrease in the lateral structural correlation length at the surface and an increase in disorder.

2. Experimental

The experiment was performed at the European Synchrotron Radiation Facility (ESRF), beamline ID03 [19] at a photon energy of 11.5 keV. The beamline is equipped with a 6-circle diffractometer and a maxipix 2D detector. A natural magnetite single crystal with a size of 10x10x2 mm^3 was mounted in a mobile UHV compatible chamber with a base pressure of $7 \cdot 10^{-9}$ mbar and the ability to work under gas flow conditions at atmospheric pressures [20]. The surface of the sample was prepared before each measurement by multiple cycles of sputtering with 1 kV Ar ions at 10^{-5} mbar Ar pressure and subsequent annealing at 920 K for 20 minutes in vacuum, with the last two annealing cycles in $2 \cdot 10^{-6}$ mbar oxygen. For the determination of the surface structure, a set of crystal truncation rods as well as surface rods was measured at a fixed angle of incidence of 2°. This was done by performing rocking scans with sample rotation axis normal to the surface at different L-values on five non-symmetry equivalent surface rods as well as seven non-symmetry equivalent crystal truncation rods. For the measurements under water vapor flow conditions, deionized water was cleaned by several freeze-pump-thaw cycles. Argon was bubbled through the water and let into the chamber at a flow of 15 ml/min, while a pressure of 100 mbar was maintained inside the reactor part of the chamber at room temperature.To simulate water-gas shift conditions, a combined flow of Ar/water vapor at a rate of 15 ml/min and CO at a rate of 20 ml/min was applied. The sample was heated by a boron nitrite encapsulated pyrolytic graphite heater and the sample temperature was obtained from a previous heating current - temperature calibration for UHV and flow conditions with an accuracy of ±20 K.

3. Results

To extract the structure factors from the measured rocking scans, the program ANA from the ANAROD-package was used. Background subtracted rocking scans were integrated and standard correction factors were applied such as Lorentz and polarization factors, area correction and the statistical error was determined [21]. Due to the fact that for surface x-ray diffraction (SXRD), in most cases, the systematic errors due to misalignment govern the total error of the measurements an additional systematic error of 15% was

introduced. Fitting of a structural model to the data was performed using the program ROD from the same package, employing the adaptive simulated annealing algorithm to avoid suboptimal local minima. The x-ray data are presented using bulk (cubic) reciprocal lattice coordinates (H,K,L) related to the reciprocal lattice vectors a^*, b^*, c^* with $a^* = b^* = c^* = 2\pi/a_0$, and $a_0 = 8.397$ Å (magnetite bulk lattice constant).

3.1. Reconstructed Surface

The bulk structure of magnetite is shown in Figure 1a. In the [001] direction, the structure is built up by so-called B layers of octahedrally coordinated iron (shown as yellow spheres) and oxygen (red spheres) and A layers of tetrahedrally coordinated iron (blue spheres). The newly proposed subsurface cation vacancy (SCV) structure model is shown in Figure 1b. In the first A layer from the surface, shown in Figure 2 a), an additional tetrahedral iron ion is added in each unit cell, while in the B layer underneath (Figure 2 b)), two iron vacancies are formed (empty black circles), resulting in one net iron ion missing per unit cell. As a starting model for the refinement of the surface structure, a model based on a refinement of LEED I-V measurements as well as one based on DFT-calculations of the SCV model [13] were used, which differ slightly in the atomic positions. The fitting was performed by optimizing the x- y and z- positions of the iron ions layer-by-layer starting at the surface layer (see Figure 2), taking in the 2D c2mm plane symmetry group into account. In addition two 90° rotational domains were included, corresponding to the two different terraces with a step height of 2.1 Å, equivalent to a quarter of the unit cell height. Due to their lower electron number as compared to Fe, oxygen ions exhibit a smaller contribution to the scattered intensity on the rods, and therefore their positions were kept fixed. Since only the displacements in the first three layers had a significant impact on the quality of the fit, the position of all deeper layers was fixed to the bulk values. Further on, a variation of the surface fraction of the reconstructed surface was allowed to take the possibility into account that not the whole sur-

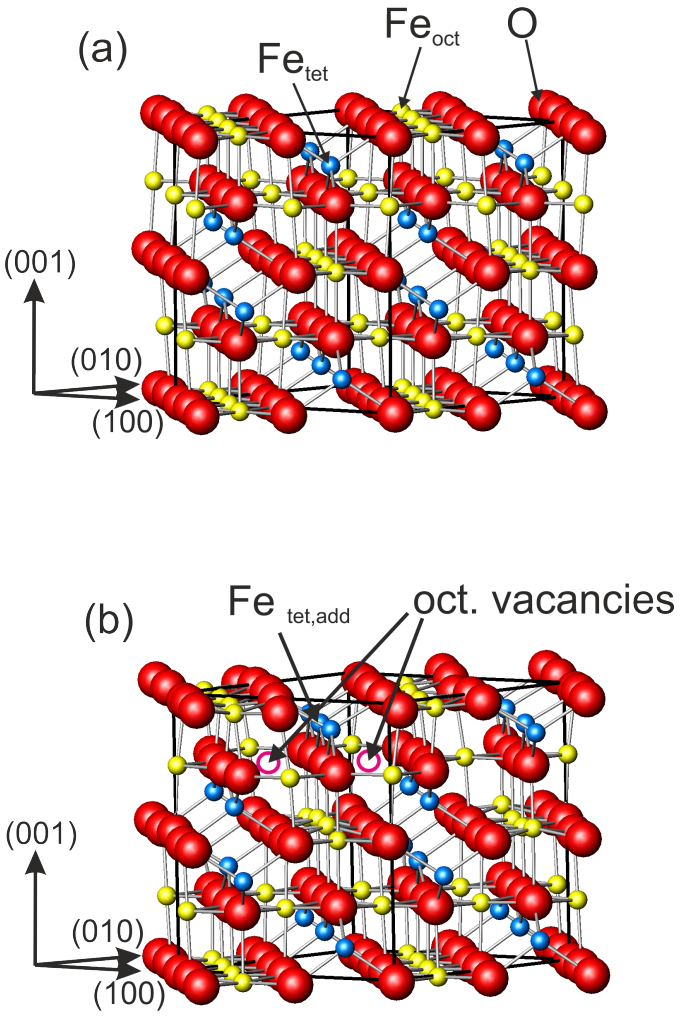

Figure 1: (a) Bulk structure of magnetite (b) Structure of the SCV model of the $\sqrt{2} \times \sqrt{2}$R45° reconstructed surface.

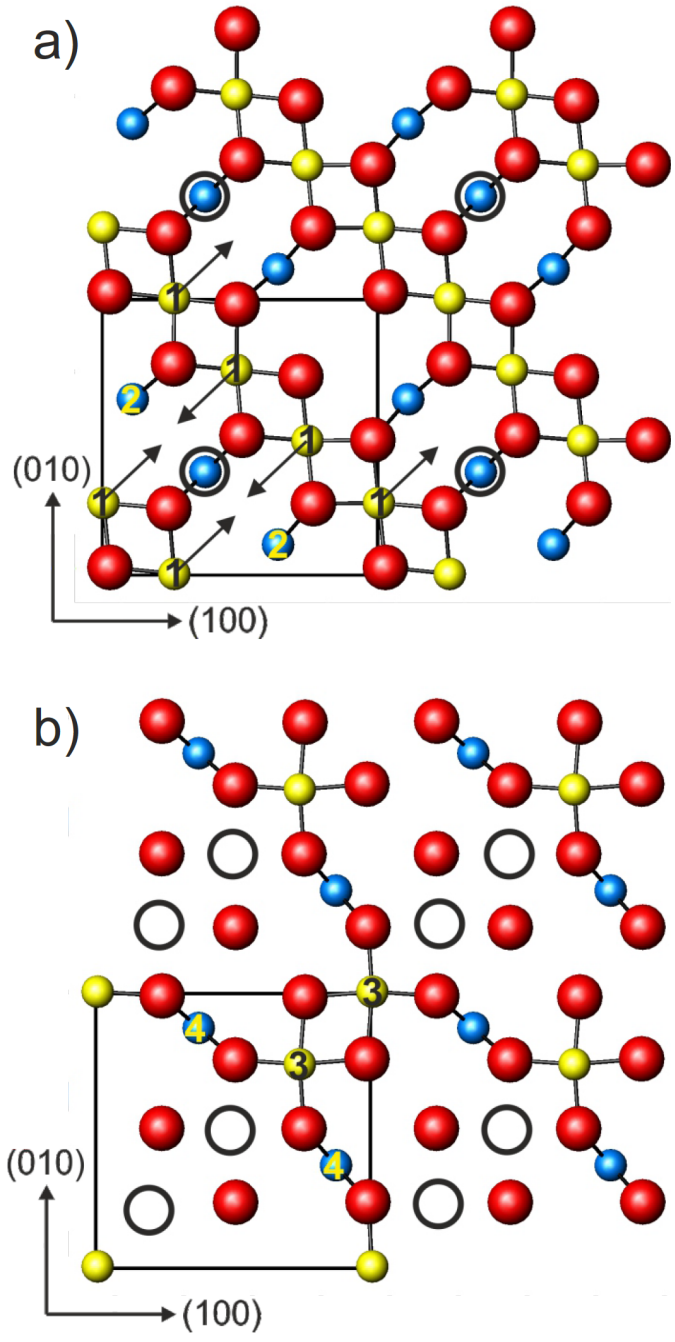

Figure 2: First (a) and second (b) layer of the subsurface cation vacancy model. The arrows mark the wave-like in-plane displacements of the iron atoms. All atoms which are included in the structural refinement are numbered according to the symmetry applied. Additional tetrahedal iron atoms and octahedral vacancies are marked with black circles.

face was reconstructed. A single scale factor for all structure factors was included. A second scale factor for the surface rods did not improve the fits or lead to any significant change in the surface fractions, and was therefore not used for the final fits. The experimental structure factors and the calculated ones from the LEED I-V based model before and after refinement [13] are shown in Figure 3, together with a comparison of structure factors for the bulk terminated DBT model [12]. The corresponding mean square weighted deviation values χ^2_{red} values characterizing the goodness of fit (see [21]) are compared in Table 1 together with the values starting the fit from LEED I-V and DFT+U atomic positions [13]. The refinements only lead to small deviations from the initial iron atom positions in the range of 0.02-0.06 Å. In the refinement of the LEED I-V based model, the deviations in the in-plane positions of the tetrahedral iron ions in the first near surface A layer as well as in the out-of-plane positions of the iron ions in the second A and B layer and the octahedral coordinated iron ions in the fourth B layer from the surface are most significant. In the refinement of the DFT-based model, the most significant change is a displacement of the iron ions towards the surface $\leq$ 0.05 Å, with some smaller changes in the in-plane positions of 0.01-0.03 Å. All changes in atomic positions are very small, reflecting the good agreement between the experimental structure factors and those calculated from the SCV model based on both LEED I-V and DFT before refinement. Small differences in the final χ^2_{red} values between both point to local nearby minima in the refinement procedure. The atom positions obtained from the refinement of the LEED I-V model can be found in the supporting material in Table A. From this, we can immediately confirm the SCV model due to its very good agreement with our data, and reject the previously proposed DBT model. According to our optimized structures, the reconstruction was covering around 76% of the surface. This may originate from residual gas adsorption of molecules in the chamber during preparation.

To examine the sensitivity of the x-ray structure factors on the reorganisation of the iron ions

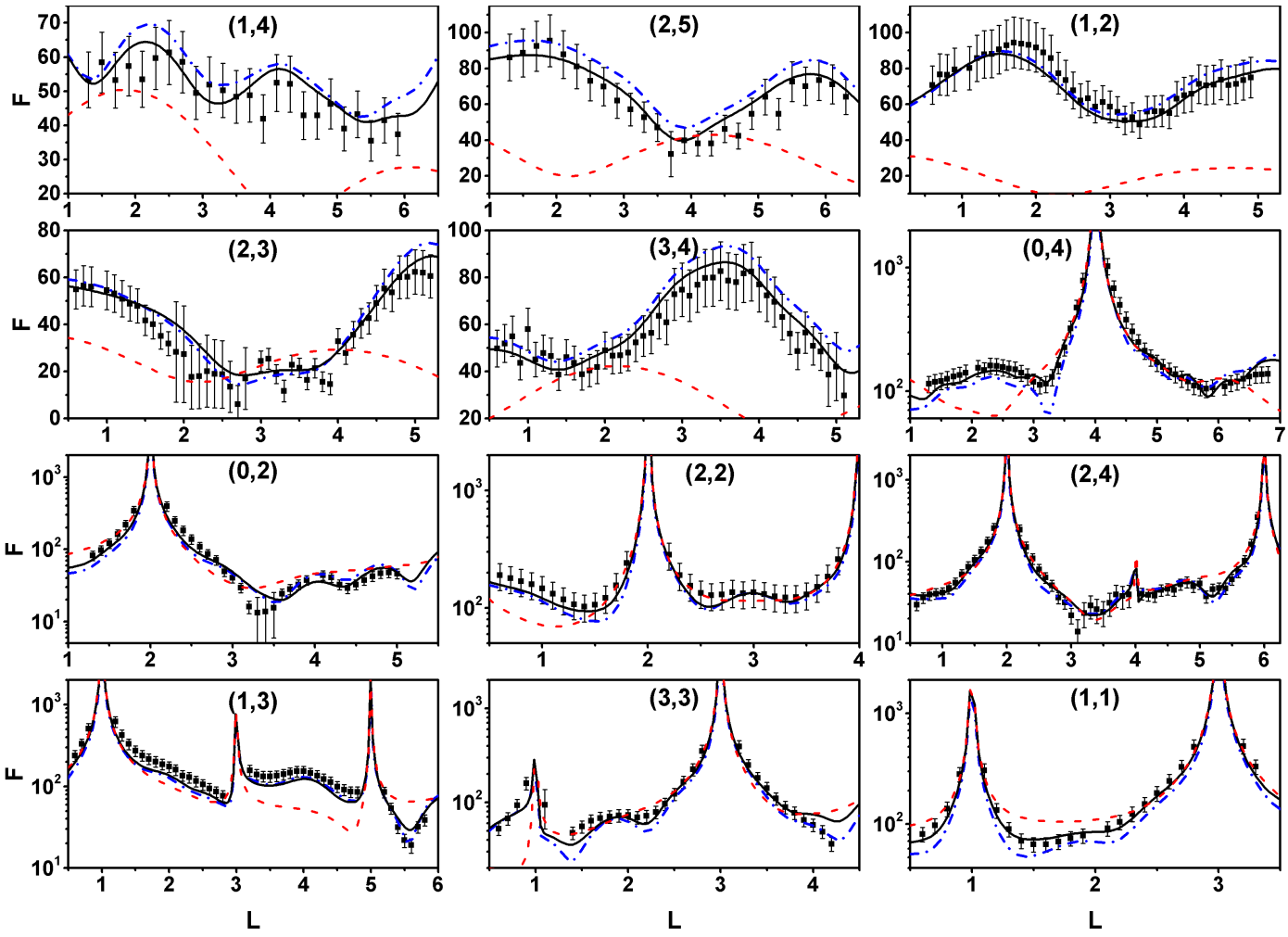

Figure 3: Comparison of x-ray structure factors F. The structure factors corresponding to the blue dot-dashed curve are calculated from the newly proposed SCV model obtained from refinement of LEED I-V measurements, the structure factors corresponding to the black curve are obtained by refining this model using the experimental SXRD structure factors. The structure factors corresponding to the formerly proposed DBT model are shown as the dashed red line for comparison. Experimental SXRD structure factors are shown as black dots together with error bars.

Model	χ^2_{red}
DBT model	8.74
SCV model, atomic positions from DFT calculations	1.97
SCV model, atomic positions from LEED I-V based refinement	1.55
Refinement of SCV model based on DFT	1.10
Refinement of SCV model based on LEED I-V	1.01

Table 1: Comparison of the mean square weighted deviations χ^2_{red} between the experimental SXRD structure factors and the structure factors calculated from the different structural models for the $\sqrt{2} \times \sqrt{2}$R45° reconstructed surface.

in the surface unit cell of the SCV model, structure factors with only the additional tetrahedral iron atom as well as only the two octahedral vacancies were calculated and scaled to the data, applying one scale factor for each model. A comparison is shown in Figure 4. Both ingredients of the reconstruction lead to distinct features in the shape of the crystal truncation rods (CTRs) and surface rods, some of which are also present in the data (like some of the oscillations on the (0,2) CTR), while some of them are missing. The (0,2) CTR is also insensitive to the filling of the octahedral vacancies in the SCV model. The (2,3)-rod around L=3 on the other hand is particularly sensitive to the occupation of the octahedral iron vacancies, with a higher occupation by iron ions giving rise to an increased structure factor around L=3.5. This leads to reduced χ^2-values of 2.42 for the model with only octahedral vacancies and 4.66 for the model with only the additional tetrahedral iron atom. Both components of the subsurface cation vacancy model therefore improve the fit, with the stronger change in stoichiometry leading to the bigger improvement. The (1,4)-rod is particularly sensitive to the surface reconstruction, with none of the components alone being able to replicate the structure factors obtained from the measurements. This shows that to model the surface reconstruction, both components are needed, as only one of them present would not lead to a structural model that fits well to the data.

3.2. Water and CO on magnetite (001)

In this section we discuss the change in atomic scale morphology of the Fe_3O_4 (001) surface under near ambient pressure water vapor and CO flow conditions for different temperatures, close to conditions for the water gas shift reaction. First the sample surface was investigated under pure water vapor / Ar flow at 15 ml / min and a total pressure of 100 mbar in the reactor part of the chamber at room temperature. The stability of the clean surface was investigated by tracking the diffraction signal of the surface reconstruction at the reciprocal lattice position (1,2,1.3). The timescan of the diffraction signal on the (1,2) rod at L=1.3 is shown in Figure 5. Upon applying the water vapor flow, the surface reconstruction was lifted in less than 10 seconds, with no signal measurable on any of the surface rods. A similar observation of reconstruction lifting upon water dosing at a much lower water vapor pressure of 10^{-6} mbar was made by LEED at 273 K [15]. The $\sqrt{2} \times \sqrt{2}$R45° reconstruction did not recover upon going back to UHV conditions, nor after subsequent heating to 570 K in UHV. This result is different to that of Mulakuluri et al. [15], who reported that heating the water exposed surface to 770 K led to a recovery of the reconstruction, which might be attributed to the lower temperature and the much higher water dosage applied in our experiment.

In the next step the sample was heated to 520 K under pure water vapor / Ar flow at 15 ml / min and a total pressure of 100 mbar. Under these conditions, the signal on the CTRs decreased significantly compared to the signal under water vapor flow without heating. This observation is characteristic for an increase in surface roughness which is also accompanied by an increase in diffuse scattering around the CTRs. By applying the beta model [22], we can estimate the increase in surface roughness from the reduction of the structure factor after water dosing at room temperature and after heating to 520 K under water vapor flow. The structure factors decreases by around 30 % at (3,3,2.7), corresponding to an increase in root mean square (r.m.s.) surface roughness of around 4.3 Å. A formation of oxygen vacancies was observed in STM [14] after low coverage water adsorption (< 0.1 monolayer) and flash annealing to 520 K in vacuum. For the water vapor induced surface roughening two scenarios are pos-

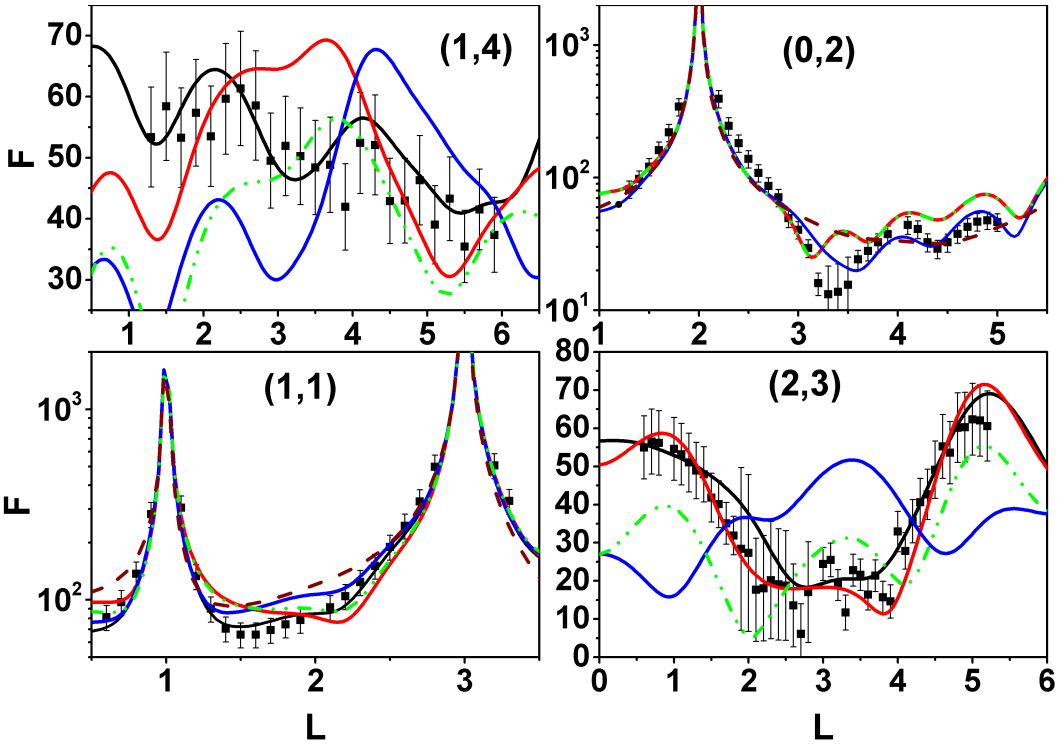

Figure 4: Comparison of experimental SXRD structure factors F (black dots) with the calculated SXRD structure factors from the fitted SCV based on LEED I-V model refinement (black line), without octahedral vacancies (blue line), without additional tetrahedral iron atom (red line), without additional tetrahedral iron atom and half of each octahedral vacancy filled (dot-dashed green line), and a bulk-truncated surface (dashed brown line).

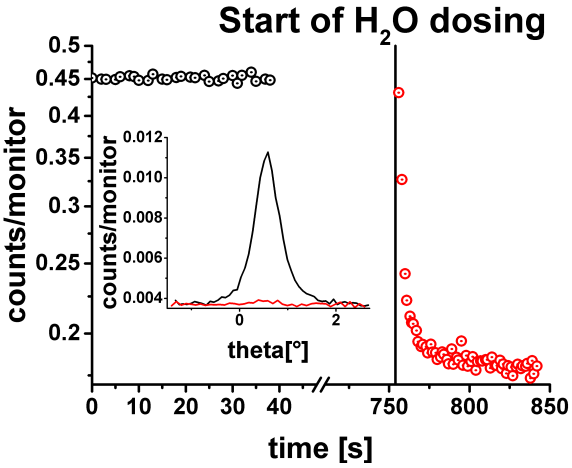

Figure 5: Timescan on the reconstruction rod at (1,2,1.3) during H_2O dosing. Theta scans on the surface rod at (1,2,1.3) before (black line) and after (red line) water dosing are shown in the inset graph confirming the complete reconstruction lifting after water dosing.

sible: either the surface continues to form oxygen vacancies by continuous surface reduction and the desorption of O_2 as proposed in [14]. In this case Fe interstitials may form, which may diffuse into the bulk, giving rise to the observed roughening. On the other hand, also the growth of iron hydroxides may take place by reaction with Fe interstitials dissolved in the bulk. It is unlikely that the formation of new stoichiometric Fe_3O_4 takes place, which was observed under the exposure to pure O_2 [23].

Applying a combined Ar/water vapor and CO flow of 15 ml/min and 20 ml/min at 520 K, respectively, while keeping the sample temperature at the same value, does not lead to any detectable changes in the surface morphology. This is supported by a comparison of the transversal (H,-K) scans on the (3,3) CTR at L=2.8 under pure water vapor flow and mixed water vapor CO flow as presented in Figure 6.

Further heating to 650 K under water-gas shift reaction conditions lead to an increase in the width

of the crystal truncation rods at (3,3,2.8) in the transversal direction along (H,K=-H) as well as a decrease in the peak intensity, thereby conserving the integrated intensity. The corresponding (H,K=-H) scan on the (3,3) CTR at L=2.8 are shown in Figure 6. The increase of the CTR profile in the transversal direction points to a lowering of the lateral correlations on the surface, such as the terrace lengths. Fitting a pseudo-Voigt profile to the data and evaluating the corresponding FWHM values leads to an average correlation length of 76 ± 5 nm at 520 K, and 29 ± 5 nm after heating to 650 K, resulting in a decrease in the in-plane surface correlation length of around 60 %. The detailed mechanism for this change in surface morphology can however not be directly inferred from our data.

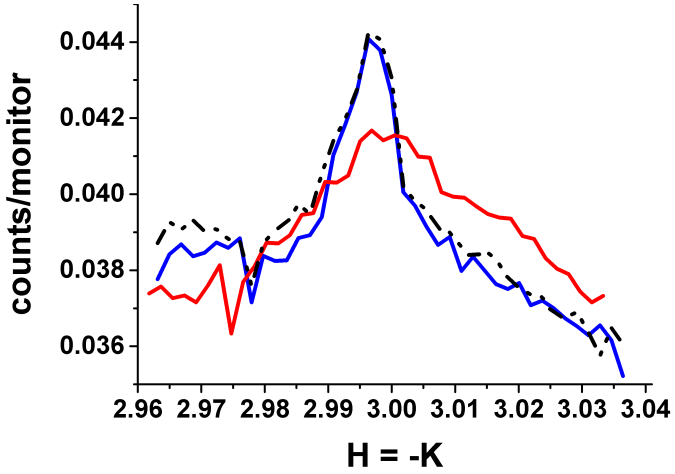

Figure 6: Monitor normalized diffracted intensity along the reciprocal (H,K=-H)-direction at (3,3,2.8) under pure water vapor / Ar flow at 520 K (dash dotted, black) line and under water-gas shift reaction conditions at 520 K (blue) and 650 K (red) sample temperature.

4. Summary and conclusion

To determine the surface structure of magnetite (001) in UHV, the surface of a natural single crystal was prepared and investigated by surface x-ray diffraction in a UHV chamber compatible with ambient pressure gas flow conditions. Based on the extensive data set we obtained on the $\sqrt{2} \times \sqrt{2}$R45° reconstructed surface, we were able to confirm and refine the subsurface cation vacancy model for the magnetite (001) $\sqrt{2}\times\sqrt{2}$R45° surface reconstruction and disprove the previously proposed distorted bulk truncation model. The refinement itself led to some small displacements of the iron atoms ($\leq$ 0.06 Å) in the first 3 layers compared to the atomic positions determined by LEED I-V experiments and DFT calculations. Utilizing SXRD, the lifting of the $\sqrt{2} \times \sqrt{2}$R45° surface reconstruction was observed upon exposing the crystal to a water vapor flow. Finally the surface was probed at elevated temperatures under water flow as well as under water-gas shift reaction conditions to obtain information about changes in the surface morphology under these conditions. At 520 K under water vapor flow, we observed an increase in the r.m.s. roughness by 4.3 Å. Upon switching to water-gas shift reaction conditions, we did not see any further changes in the roughness perpendicular to the surface, but we were able to observe a shrinking of the in-plane correlation length of the surface structure by 60% when heating the surface from 520 K to 650 K. Our experiments demonstrate that oxide surfaces under catalytic reaction conditions can undergo strong restructuring, which needs to be taken into account for an atomic scale understanding of reaction mechanisms.

Acknowledgements

We thank the technical staff from ID03 (ESRF) for their support and help during the beamtime. The German Science Foundation (DFG) is acknowledged for funding under project no. STI 554/1-1. GSP, RB, and OG acknowledge support from the Austrian Science Fund START prize Y 847-N20 and project number P24925-N20.

References

[1] C. Ratnasamy, J. P. Wagner, Catalysis Reviews 51 (3) (2009) 325–440. doi:10.1080/01614940903048661.

[2] S. Li, G. D. Meitzner, E. Iglesia, The Journal of Physical Chemistry B 105 (24) (2001) 5743–5750. doi:10.1021/jp010288u.

[3] F. dos Santos Coelho, J. D. Ardisson, F. C. Moura, R. M. Lago, E. Murad, J. D. Fabris, Chemosphere 71 (1) (2008) 90–96. doi:10.1016/j.chemosphere.2007.10.016.

[4] W. Eerenstein, T. T. M. Palstra, S. S. Saxena, T. Hibma, Physical Review Letters 88 (24) (2002) 247204. doi:10.1103/PhysRevLett.88.247204.

[5] M. E. Fleet, Journal of Solid State Chemistry 62 (1) (1986) 75–82. doi:10.1016/0022-4596(86)90218-5.

[6] G. Tarrach, D. Bürgler, T. Schaub, R. Wiesendanger, H.-J. Güntherodt, Surface Science Letters 285 (1-2) (1993) A307. doi:10.1016/0167-2584(93)90341-F.

[7] J. Gaines, P. Bloemen, J. Kohlhepp, C. Bulle-Lieuwma, R. Wolf, a. Reinders, R. Jungblut, P. van der Heijden, J. van Eemeren, J. de Stegge, W. de Jonge, Surface Science 373 (1997) 85–94. doi:10.1016/S0039-6028(96)01145-4.

[8] B. Stanka, W. Hebenstreit, U. Diebold, S. a. Chambers, Surface Science 448 (1) (2000) 49–63. doi:10.1016/S0039-6028(99)01182-6.

[9] S. Chambers, S. Thevuthasan, S. Joyce, Surface science 450 (2000) 273–279. doi:10.1016/S0039-6028(00)00230-2.

[10] G. S. Parkinson, Surface Science Reportdoi:10.1016/j.surfrep.2016.02.001.

[11] R. Pentcheva, F. Wendler, H. L. Meyerheim, W. Moritz, N. Jedrecy, M. Scheffler, Physical Review Letters 94 (12) (2005) 126101. doi:10.1103/PhysRevLett.94.126101.

[12] R. Pentcheva, W. Moritz, J. Rundgren, S. Frank, D. Schrupp, M. Scheffler, Surface Science 602 (7) (2008) 1299–1305. doi:10.1016/j.susc.2008.01.006.

[13] R. Bliem, E. McDermott, P. Ferstl, M. Setvin, O. Gamba, J. Pavelec, M. A. Schneider, M. Schmid, U. Diebold, P. Blaha, L. Hammer, G. S. Parkinson, Science 346 (6214) (2014) 1215–1218. doi:10.1126/science.1260556.

[14] G. S. Parkinson, Z. Novotný, P. Jacobson, M. Schmid, U. Diebold, Journal of the American Chemical Society 133 (32) (2011) 12650–5. doi:10.1021/ja203432e.
URL http://www.ncbi.nlm.nih.gov/pubmed/21740022

[15] N. Mulakaluri, R. Pentcheva, M. Wieland, W. Moritz, M. Scheffler, Physical Review Letters 103 (17) (2009) 1–4. doi:10.1103/PhysRevLett.103.176102.

[16] T. Kendelewicz, P. Liu, C. Doyle, G. Brown, E. Nelson, S. Chambers, Surface Science 453 (1-3) (2000) 32–46. doi:10.1016/S0039-6028(00)00305-8.

[17] T. Kendelewicz, S. Kaya, J. T. Newberg, H. Bluhm, N. Mulakaluri, W. Moritz, M. Scheffler, A. Nilsson, R. Pentcheva, G. E. Brown, The Journal of Physical Chemistry C 117 (6) (2013) 2719–2733. doi:10.1021/jp3078024.
URL http://pubs.acs.org/doi/full/10.1021/jp3078024http://pubs.acs.org/doi/abs/10.1021/jp3078024

[18] N. Mulakaluri, R. Pentcheva, M. Scheffler, The Journal of Physical Chemistry C 114 (25) (2010) 11148–11156. doi:10.1021/jp100344n.
URL http://dx.doi.org/10.1021/jp100344n

[19] O. Balmes, R. van Rijn, D. Wermeille, A. Resta, L. Petit, H. Isern, T. Dufrane, R. Felici, Catalysis Today 145 (2009) 220–226. doi:10.1016/j.cattod.2009.02.008.

[20] R. Van Rijn, M. D. Ackermann, O. Balmes, T. Dufrane, a. Geluk, H. Gonzalez, H. Isern, E. De Kuyper, L. Petit, V. a. Sole, D. Wermeille, R. Felici, J. W. M. Frenken, Review of Scientific Instruments 81 (1). doi:10.1063/1.3290420.

[21] E. Vlieg, Journal of Applied Crystallography 33 (2000) 401–405. doi:10.1107/S0021889899013655.

[22] I. K. Robinson, Physical Review B 33 (6) (1986) 3830–3836. doi:10.1103/PhysRevB.33.3830.

[23] S. Nie, E. Starodub, M. Monti, D. A. Siegel, L. Vergara, F. El Gabaly, N. C. Bartelt, J. De La Figuera, K. F. McCarty, Journal of the American Chemical Society 135 (27) (2013) 10091–10098. doi:10.1021/ja402599t.

Supporting Material

Atom	LEED			DFT			Fit		
	x	y	z	x	y	z	x	y	z
O	0.98301	0.49049	0.89421	0.9812	0.4898	0.8925	0.98301	0.49049	0.89421
O	0.25951	0.76699	0.89421	0.2571	0.7658	0.8928	0.25951	0.76699	0.89421
O	0.49049	0.98301	0.89421	0.4884	0.9825	0.8925	0.49049	0.98301	0.89421
O	0.76699	0.25951	0.89421	0.7645	0.2585	0.8925	0.76699	0.25951	0.89421
Fe	0.48796	0.74508	0.86381	0.4856	0.7407	0.8662	0.48889	0.74618	0.86538
Fe	0.26204	0.00492	0.86381	0.2598	0.0074	0.8660	0.26111	0.00382	0.86538
Fe	0.00492	0.26204	0.86381	0.0062	0.2612	0.8661	0.00382	0.26111	0.86538
Fe	0.74508	0.48796	0.86381	0.7395	0.4869	0.8659	0.74618	0.48889	0.86538
O	0.24223	0.24223	0.8954	0.2412	0.2424	0.8931	0.24223	0.24223	0.8954
O	0.02853	0.02853	0.87394	0.0263	0.0278	0.8744	0.02853	0.02853	0.87394
O	0.50777	0.50777	0.8954	0.5045	0.5056	0.8930	0.50777	0.50777	0.8954
O	0.72147	0.72147	0.87394	0.7191	0.7204	0.8748	0.72147	0.72147	0.87394
Fe	0.63886	0.11114	0.78572	0.6369	0.11	0.7873	0.63674	0.11326	0.78441
Fe	0.11114	0.63886	0.78572	0.1088	0.6383	0.7876	0.11326	0.63674	0.78441
Fe	0.375	0.375	0.77618	0.373	0.3737	0.7767	0.375	0.375	0.77878
O	0.50819	0.75856	0.63729	0.5069	0.7592	0.6376	0.50819	0.75856	0.63729
O	-0.00856	0.24181	0.63729	-0.0121	0.2404	0.6373	-0.00856	0.24181	0.63729
O	0.75856	0.50819	0.63729	0.7582	0.5084	0.6372	0.75856	0.50819	0.63729
O	0.24181	-0.00856	0.63729	0.2387	-0.0107	0.6374	0.24181	-0.00856	0.63729
Fe	0.74297	0.74297	0.64504	0.7407	0.7425	0.6476	0.74335	0.74335	0.64139
Fe	0.00703	0.00703	0.64504	0.0048	0.0065	0.6469	0.00665	0.00665	0.64139
O	0.76236	0.98764	0.63849	0.7583	0.9887	0.6357	0.76236	0.98764	0.63849
O	0.24054	0.50946	0.64862	0.2399	0.5074	0.6487	0.24054	0.50946	0.64862
O	0.98764	0.76236	0.63849	0.9872	0.7599	0.6363	0.98764	0.76236	0.63849
O	0.50946	0.24054	0.64862	0.5063	0.2407	0.6479	0.50946	0.24054	0.64862
Fe	0.87493	0.375	0.50794	0.8734	0.3746	0.5104	0.87459	0.37534	0.51447
Fe	0.375	0.87493	0.50794	0.3729	0.8743	0.5106	0.37534	0.87459	0.51447
O	0.49091	0.49091	0.39111	0.4862	0.486	0.3873	0.49091	0.49091	0.39111
O	0.75266	0.75266	0.39945	0.7553	0.7565	0.3999	0.75266	0.75266	0.39945
O	0.99734	0.99734	0.39945	0.9901	0.9923	0.3986	0.99734	0.99734	0.39945
O	0.25909	0.25909	0.39111	0.2604	0.2616	0.3897	0.25909	0.25909	0.39111
Fe	0.49513	0.25487	0.41972	0.4922	0.2532	0.4194	0.49439	0.25561	0.42182
Fe	0.75308	-0.00308	0.39528	0.7456	0	0.3961	0.75382	-0.00382	0.39738
Fe	0.25487	0.49513	0.41972	0.2547	0.494	0.4207	0.25561	0.49439	0.421822
Fe	-0.00308	0.75308	0.39528	-0.0015	0.7489	0.3975	-0.00382	0.75382	0.39738
O	0.00956	0.5044	0.38574	0.01	0.5084	0.3864	0.00956	0.5044	0.38574
O	0.5044	0.00956	0.38574	0.5063	0.0097	0.3856	0.5044	0.00956	0.38574
O	0.74044	0.2456	0.38574	0.7374	0.2405	0.3867	0.74044	0.2456	0.38574
O	0.2456	0.74044	0.38574	0.2388	0.7378	0.3879	0.2456	0.74044	0.38574
Fe	0.1318	0.1318	0.27249	0.1255	0.13	0.2763	0.1318	0.1318	0.27206
Fe	0.6182	0.6182	0.27249	0.6214	0.6194	0.2761	0.6182	0.6182	0.27206

O	0.00535	0.74465	0.150327	-0.0032	0.7431	0.1561	0.00535	0.74465	0.15327
O	0.74465	0.00535	0.15327	0.7413	0.0069	0.1548	0.74465	0.00535	0.15327
O	0.2456	0.5044	0.15208	0.2418	0.4989	0.1501	0.2456	0.5044	0.15208
O	0.5044	0.2456	0.15208	0.5084	0.2399	0.1509	0.5044	0.2456	0.15208
Fe	0.00324	0.49976	0.14313	0.0075	0.5	0.1426	0.00324	0.49976	0.14313
Fe	0.74676	0.25024	0.14313	0.7445	0.2534	0.1428	0.74676	0.25024	0.14313
Fe	0.25024	0.74676	0.14313	0.2481	0.7459	0.1454	0.25024	0.74676	0.14313
Fe	0.49976	0.00324	0.14313	0.4902	-0.0051	0.1384	0.49976	0.00324	0.14313
O	0.99228	0.25277	0.14612	0.9886	0.257	0.1485	0.99228	0.25277	0.14612
O	0.25277	0.99228	0.14612	0.2535	0.9985	0.1478	0.25277	0.99228	0.14612
O	0.49723	0.75772	0.14612	0.4991	0.756	0.1479	0.49723	0.75772	0.14612
O	0.75772	0.49723	0.14612	0.7579	0.4917	0.1479	0.75772	0.49723	0.14612
Fe	0.375	0.375	0.02749	0.3756	0.3712	0.0254	0.375	0.375	0.02749
Fe	0.87498	0.87502	0.02272	0.8708	0.8751	0.0246	0.87498	0.87502	0.02272

Table A: Atomic positions of the three models in coordinates relative to the experimental magnetite bulk lattice constant $a_0 = 8.397$ Å.